Aerodynamic Characteristics of Flapping Motion in Hover

D. Funda Kurtulus[1,4], Laurent David[2], Alain Farcy[3], Nafiz Alemdaroglu[4]

1: LEA, ENSMA, Poitiers, France, dfunda@ae.metu.edu.tr
2: LEA, University of Poitiers, Poitiers, France, Laurent.David@univ-poitiers.fr
3: LEA, ENSMA, Poitiers, France, farcy@ensma.fr
4: Department of Aerospace Engineering, METU, Ankara, Turkey, nafiz@metu.edu.tr

Abstract The aim of the present study is to understand the aerodynamics phenomena and the vortex topology of the highly unsteady flapping motion by both numerical and experimental solutions. Instead of the use of real insect/bird wing geometries and motions which are highly complex and difficult to imitate by an exact modeling, a simplified model is used to understand the unsteady aerodynamics and vortex formation during the different phase of the flapping motion. The flow is assumed to be laminar with the Reynolds number of 1,000. The experimental results obtained by the laser sheet visualization and the Particle Image Velocimetry (PIV) techniques are used for the phenomenological analysis of the flow. The vortex dynamics is put in evidence and explained with the use of different tools. Vortex identification from PIV measurements is performed by considering velocity magnitude, streamlines, second invariant of velocity gradient (Q-criteria), vorticity contours and Eulerian accelerations.

1. Introduction

The numerical and experimental studies of low Re number regime become very important due to the advances in micro-technologies enabling the development of Micro Air Vehicles (MAV's). One of the main objectives of MAV applications, i.e. constant position surveillance, reveals the need to focus the researches on hover mode. There are three generation of MAV's namely fixed wings, rotating wings (like helicopters) and wings based on micro technology (MEMS, flapping or vibrating wings). The definition employed in Defense Advanced Research Projects Agency (DARPA) program limits these craft to a size less than 15 cm in length, width or height. This physical size puts this class of vehicle at least an order of magnitude smaller than any UAV developed to date.

The studies on flapping motion flight can be classified into two main parts as the zoological configurations and the simplified configurations. Zoological configuration studies are performed based on the study of the insects or birds. Comprehensive reviews of the biological flight mechanisms could be found in Nachtigall (1974); Rayner (1979, 1985); Ellington (1984); Norberg (1985); Azuma et al. (1985); Pennycuick (1988) and Dudley (1998).

The simplified configurations are mostly the studies based on the aerodynamics of the flow. The models are simplified such that different profiles are used instead of the real insect/bird wing geometries (Shyy et al. 1999; Ramamurti and Sandberg 2002; Platzer and Jones 2006). Although most of the researches are performed with numerical simulations, it is highly difficult to solve the full 3D Navier–Stokes equations for unsteady flows around insect wings. Hamdani and Sun (2000) simulated a series of impulsive starts at different accelerations around a 2D insect wing. The mean streamwise velocity field of the wake of a NACA 0012 airfoil oscillating in plunge at zero freestream velocity and at a zero angle of incidence at the neutral position was calculated by Lai and Platzer (2001). The vortical flow patterns in the wake of a NACA 0012 airfoil pitching at small amplitudes are studied by Koochesfahani (1989) in a low-speed water channel by considering the effect of both sinusoidal and non-sinusoidal shape of the waveform.

Dickinson (1994) experimentally observed that four important parameters of stroke reversal

influenced the generation of the force during the subsequent stroke. These are the position of the rotational axis, the speed of rotation, the angle of attack of the preceding stroke and the length of the preceding stroke. The motion of the wing profile was divided into three temporally distinct phases: the first translation (downstroke), wing rotation and the second translation in the opposite direction from the first (upstroke). The present study is concerned with a similar motion in hover mode, where the free-stream velocity is zero. In hovering, the main effect is to produce a vertical force in order to balance the weight. Hummingbird and several insects use normal hovering where the wings are moving through a large angle in an approximately horizontal plane making a figure-of-eight motion with a symmetrical half-strokes.

During this study, it was necessary to simplify the problem in order to understand the complex unsteady aerodynamics of the flapping motion. Therefore, the numerical simulations and experimental setup are performed in 2D. A simplified motion is proposed for the flapping mechanism with continuous velocities. The following section will explain the definition of the motion, the numerical tools and the experimental setup. A reference configuration is chosen to study the topology of the flow. And finally, the physical analysis is performed with a discussion on the instantaneous aerodynamic forces, pressure coefficients and Eulerian accelerations at different phases of the motion.

2. Numerical and experimental tools

2.1 Definition of the flapping motion

The model is simplified by use of a symmetrical airfoil (NACA 0012), so that the symmetry of the motion both during upstroke and downstroke is not lost. The flapping motion is simulated with the superposition of a translational motion and a rotational motion around a center of rotation. During the translational phase, the airfoil translates with a constant velocity until the time t_v and position x_v, where a rotational motion around a point on the chordline is superposed to the translational motion at a predefined time t_a and position x_a. The translational velocity is zero ($V = 0$) at the end of the strokes. After the time t_a and the position x_a, the airfoil starts to rotate around the center of rotation where it reaches 90° angle of attack at the quarter period. The rotation is such that the leading edge stays as leading edge during all phases of the motion. The translational velocity (V) and the angular velocity (ω) variation are given by Eq. 1 and Eq. 2. The continuity of the velocities is conserved by these proposed motions.

$$V = V_0 \cos\left(\frac{\pi}{2}\frac{t - t_v}{\frac{T}{4} - t_v}\right) \tag{1}$$

$$\omega = -\frac{\alpha_0}{\frac{T}{4} - t_a}\left(1 - \cos\left(\frac{\pi(t - t_a)}{\frac{T}{4} - t_a}\right)\right) \tag{2}$$

where V_0 is the constant translational velocity, α_0 is the constant angle of attack and T is the period of the motion.

The flapping motion is divided into 4 regions with the first region corresponding to the half of the downstroke. Second region represents the half-upstroke. The third and fourth regions are the mirror images of these two regions, corresponding to the second half of upstroke and downstroke respectively. Each half cycle starts from rest and comes to a stop. The total displacement of the airfoil is 6 chord. Figure 1 shows detailed description of the flapping motion in one period. The

influences of the angle of attack α_0, the position of the velocity change x_v, the position of the angle of attack change x_a, the center of rotation position and Re number are investigated with experimental and numerical means. For this study, one of these cases is chosen in order to represent topological investigations and physical interpretations of this unsteady complex motion.

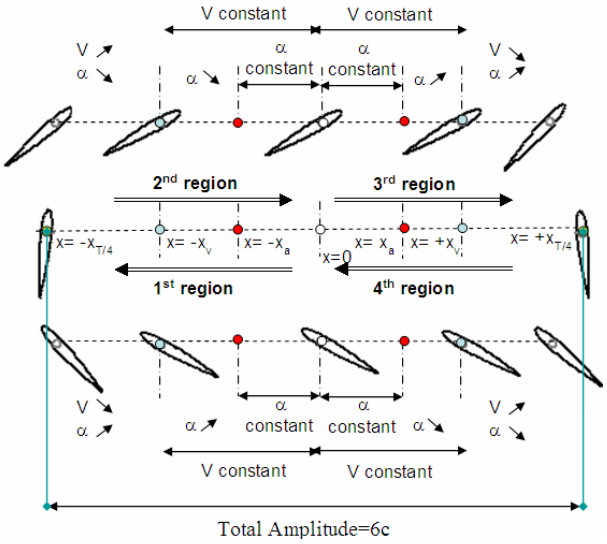

Fig. 1 Flapping motion definition

2.2 Numerical tools

The unsteady, 2D, laminar flow equations are used to compute the flowfield using Star-CD, a Direct Numerical Simulation (DNS) code. The program use implicit methods to solve the algebraic finite-volume equations. The proposed flapping motion is implemented with user-defined subroutines by moving the whole computational domain (Kurtulus et al. 2005). On the airfoil surface, the instantaneous translational and rotational velocities are prescribed; imposing no-slip, no-penetration boundary conditions. At the far-field, the pressure boundary conditions are applied. In hover condition, the far-field pressure is assumed to be the standard air pressure. The velocities at the corresponding cell faces are linked to the local pressure gradients by special momentum equations. These equations, together with the continuity constraint, effectively allow the magnitude and direction of the local flow of the far-field. For 2D calculations, the front and back side of the grid domain are defined as symmetric boundary conditions. O-type grid with 20c far-field radius is used around the airfoil with a finer grid domain close to the airfoil and a coarser grid domain at the far-field. The arbitrary mesh-interface option is used to join dissimilar mesh structures, in order to decrease the number of cells at the far-field locations. A grid domain of 57500 cells was used for the computation of 7000 iteration with a time step of 10^{-4} s.

2.3 Experimental setup

A rectangular wing with a NACA 0012 airfoil section is displaced in a tank filled with water by associating a rotational and a translational motion. The experimental setup is a 1.5 m×1 m×1 m water tank made of altuglas. The wing is delimited by two rectangular plates made of epoxy with 50 cm×90 cm dimensions in order to obtain a 2D flow (Fig. 2). The wing is free to rotate relative to the plates. The chord length, c, of the wing is 6 cm and the span is 50 cm. The centre of rotation is at c/4 location of the airfoil. The system consists of 2 step motors. The first motor is a high torque brushless motor associated with an endless screw allowing the translational motion with a maximum linear velocity of 4 cm/s. The second one, associated with 2 pulleys allows the rotation of the profile. The useful distance of the translational motion is 600 mm and that of the rotational is of 360^o. The flapping motion is carried out in zero free-stream velocity. A laminar flow is generated

with a Reynolds number of 1,000 calculated with respect to the chord and the maximum velocity of the motion. The total displacement of the airfoil is fixed to 6c and the angular displacement is from α= -45° to 45° for this particular study. The system is controlled with variable velocity in open loop using a computer with a real time data acquisition. The generated signal is also used for the synchronizations of image acquisition. The seeding is done by using micro-spherical hollow particles of glass silver plated on the surface with a mean diameter of 15 µm. The concentration of the particles in the whole volume of the water tank is approximately $V_{particle}/V_{tank} = 1.9 \cdot 10^{-6}$.

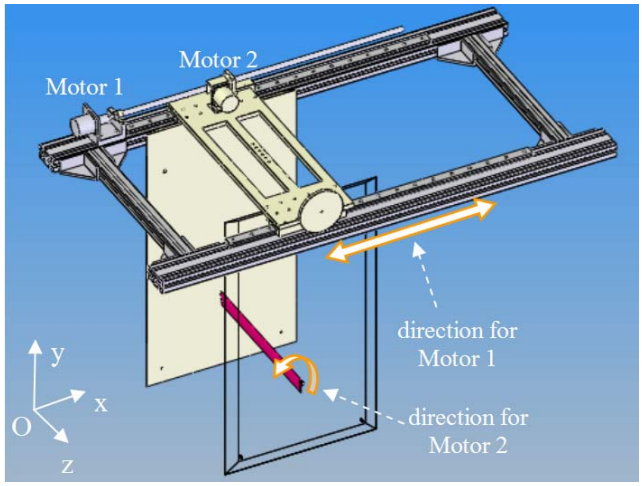

Fig. 2 Schematic diagram of the experimental setup

For the laser sheet visualization, the median section of the wing is illuminated by a continuous laser system (Argon Spectra-Physics of 10W maximum capacity) coupled with two spherical lenses of focal distance 50 mm, followed by a cylindrical lens. The direction of the luminous plan is adjusted to be parallel to the flapping motion direction. At the back side of the water tank, a mirror of 100 mm × 1500 mm is inserted in order to illuminate the flow field on top of the airfoil to limit the airfoil's shadow. To record the flow, a NIKON-MB-21 F4S camera with a 60 mm objective is placed perpendicular to the laser sheet. The exposure time of 500 ms and F number of 8 are chosen for the visualization study. The non-dimensional time t* is defined as:

$$t^* = \frac{V_P \cdot t}{c} \qquad (3)$$

where $V_p = c/\overline{T}$ and $\overline{T}$ is the average period found by repeating three times the experiment during 12 periods. The camera is synchronized to obtain the non dimensional time interval $\Delta t^* = 0.04$.

Particle Image Velocimetry (PIV) measurements are performed with a 30 mJ pulsed Quantel Twin Ultra Nd:YAG laser coupled with a spherical lens followed by a cylindrical lens. A mirror is located at the bottom center of the water tank to spread the light of the laser to the whole flow domain as wide as possible and to limit the shadow generated by the model. Two intensified CCD cameras with 60 mm objectives and F number of 4 are used to record the entire flow domain with a field of view of 25 cm × 50 cm. The acquisition is synchronized with the motion. The external trigger time of the images is chosen to take 80 double frames per period for each camera. The exposure delay time is 81300 µs which corresponds to the separation between the two laser flashes to have a displacement of about 8 pixels. Double frame/double exposure and cross-correlation are applied as the interrogation method using adaptive multi pass with window deformation. The interrogation window size initiates from 64 ×64 pixels and ends with a final interrogation window size of 32 × 32 pixels with an option 50% overlap of the final window. The case α_0= 45°, x_v= 2c, x_a= 2c is chosen as a reference configuration with a period of 51.4 s. Instantaneous velocity measurements, streamlines, vorticity, second invariant of velocity gradient (Q-criteria), Eulerian accelerations are calculated to identify different types of vortices.

3. Topology and time evaluation of the flow

The two experiments namely laser sheet visualization and Particle Image Velocimetry (PIV) are used in this section in view of vortex identification and flow topology. The flow is investigated for the 7th period. At this time interval, the influence of the impulsive start is negligible and all the vortices observed at the time t*= 1.00 (representing the beginning of the 8th period) are also similarly visible at the time t*= 0 (representing the beginning of the 7th period). This also proves the periodic vortex topology of the motion. The topology analysis is determined by the streamlines obtained from visualizations or calculated from velocity field of PIV measurements. The vorticity and Q values are non-dimensionalized with the chord of the airfoil and the constant translational velocity, V_0.

During a period, three types of vortices are generated: Leading Edge Vortex (LEV) at the leading edge of the airfoil, Translational Vortex (TV) at the trailing edge of the airfoil and Rotational Stopping Vortex (RSV) similarly at the trailing edge of the airfoil. The LEV and TV are the vortices generated during the translation of the airfoil and RSV is generated due to the rotation of the airfoil and detach from the airfoil at the return. Nomenclature of the vortices visualized during the flapping motion is given in Table 1 with their corresponding description, location of the formation (at the leading edge or at the trailing edge of the airfoil) and the generation phases (during translational or rotational phases).

Table 1 Nomenclature of the vortices generated during the flapping motion.

Vortex Type	**Description** (LE: leading edge, TE: trailing edge)	**Vortex Generation Phase**
LEV1	Leading Edge Vortex 1, LE	Before translational phase starts
LEV2	Leading Edge Vortex 2, LE	At the beginning of translational phase
TV1	Translational Vortex 1, TE	Before translational phase starts
LEV3	Leading Edge Vortex 3, LE	During pure translation
TV2	Translational Vortex 2, TE	During pure translation
TV3	Translational Vortex 3, TE	At the mid-section of the translational phase
LEV4	Leading Edge Vortex 4, LE	At the beginning of rotational phase
LEV5	Leading Edge Vortex 5, LE	At the end of the rotational phase
RSV1	Rotational Stopping Vortex 1, TE	At the end of the rotational phase

The cores of the vortices are represented with points at the particle visualizations (Fig. 3). The blue colors represent the clockwise vortices and the red colors represent the counter-clockwise vortices. Figure 4 shows streamlines obtained from the PIV measurements at the same time instants as the laser sheet visualizations in Fig. 3. The explanation of the motion is started close to the end of the rotational phase. Until the constant velocity translational phase, there is a formation of a counter-clockwise leading edge vortex (LEV1) which detaches very quickly from the surface of the airfoil, leaving its place to a newly generated leading edge vortex, LEV2. At the beginning of the translation (t*= 0.08), this counter-clockwise LEV2 starts to be visualized clearly. In the mean time, a clockwise translational vortex, TV1 is formed. All remaining vortices shown at t*= 0.08 (represented in yellow color in Fig. 3) are the trace of the vortices generated during the previous period. At t*= 0.12, LEV2 grows with the translation of the airfoil, remaining always attached to it. In the meantime, LEV1 is separated from the airfoil upper surface and the translational vortex TV1 is started to detach from the airfoil. As the airfoil translates, the translational vortex TV1 stretches and left always a wake behind the airfoil until the mid-amplitude of the motion.

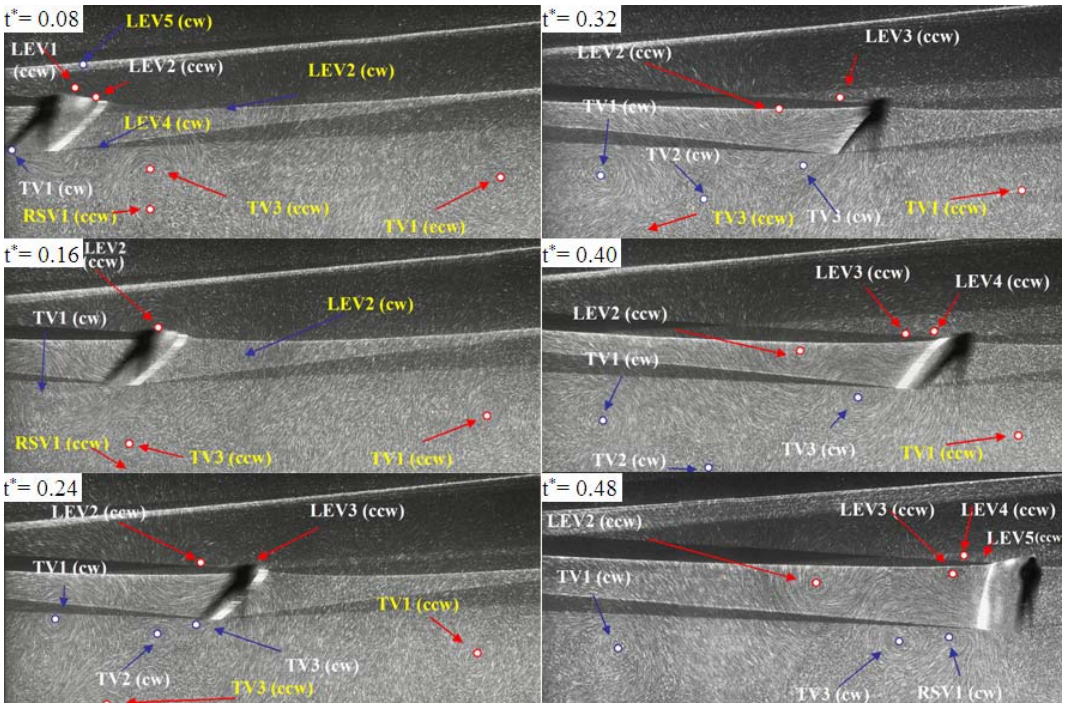

Fig. 3 Instantaneous vortex topology by laser sheet visualization

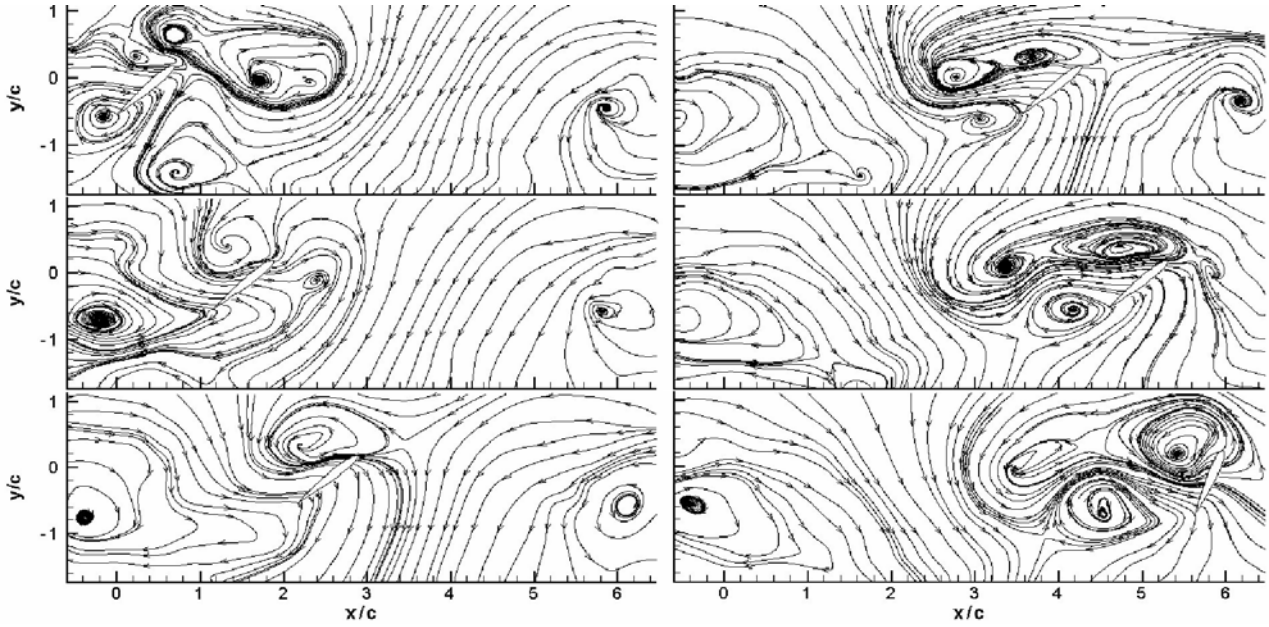

Fig. 4 Instantaneous streamlines from PIV measurements

Figure 5 shows the instantaneous non-dimensional vorticity and Q contours for the same time instants as Fig. 3 and Fig. 4. The vorticity contours reveals the direction of the vortices, which are counter-clockwise in the positive region (red) and clockwise in the negative region (blue) as shown in Fig. 5. *Q* is the balance between the rotation rate and the strain rate. The positive Q iso-surfaces isolate areas where the strength of rotation overcomes the strain rate, thus making those surfaces eligible as vortex envelopes. Since vorticity should increase as the centre of the vortex is approached, *Q* can be expected to remain positive (red regions in Fig. 5) in the core of the vortex. Negative *Q* values imply a shear region. There is a very thick shear region in front of the airfoil at t*= 0.08, which seems to be due to the interaction between the airfoil and the vortices generated during previous stroke (Fig. 5-*top right*). LEV2 gets bigger and bigger during the translational phase of the motion at t*= 0.24 (Figs. 3-5). At the same time, a new translational vortex TV3 is

formed. A big trace of the vortices is formed at the back side of the airfoil from the combination of the vortices TV1 and TV2. At t*= 0.28, the leading edge vortex LEV2 detaches fro the airfoil surface. At t*= 0.32 the translational vortex TV3 is highly visible. At t*= 0.36, the new leading edge vortex LEV4 is formed. The LEV3 and TV3 are almost occupying half by half of the airfoil upper surface in inertial frame of reference.

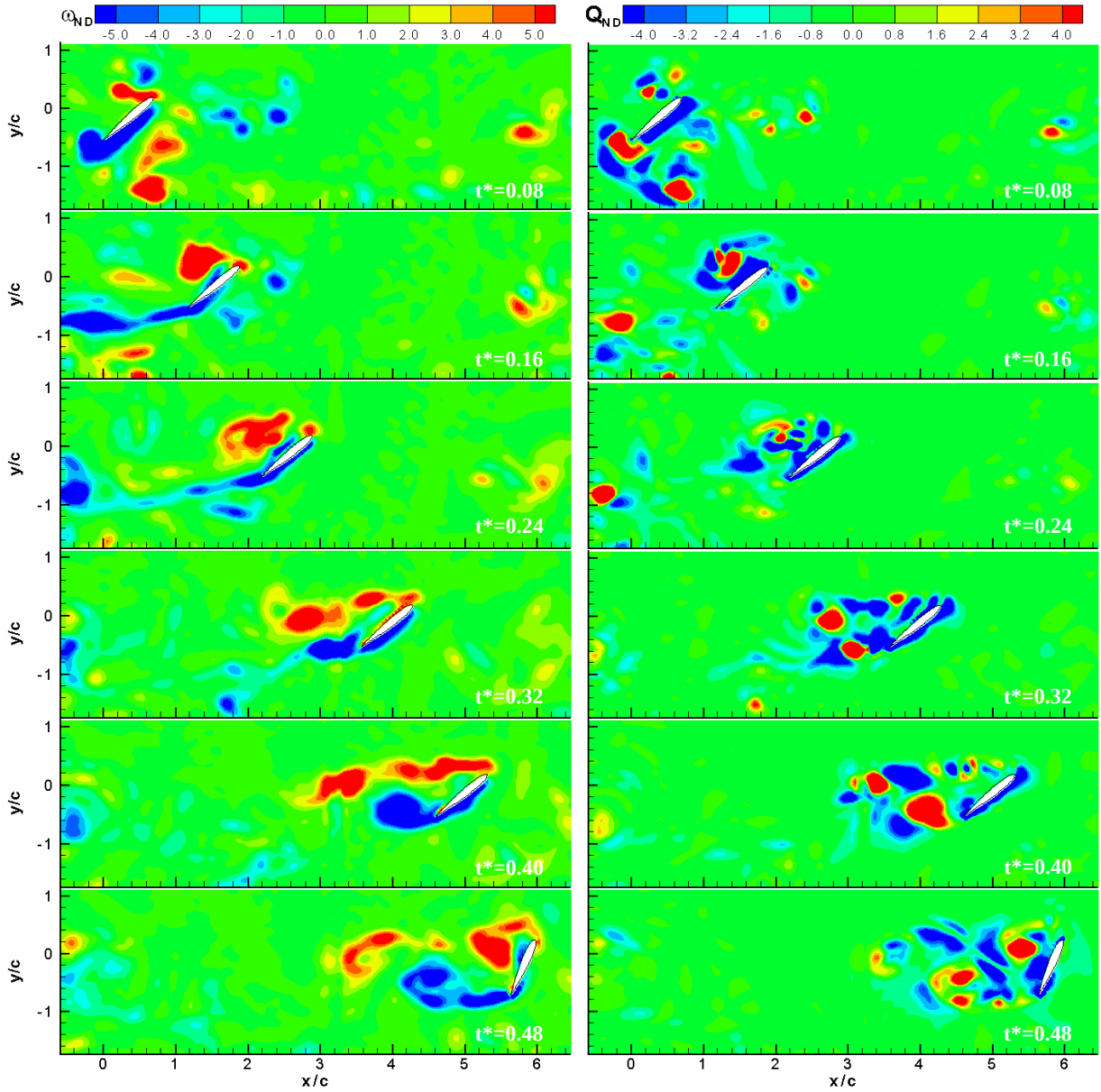

Fig. 5 Instantaneous non-dimensional vorticity (*left column*) and Q contours (*right column*) from PIV measurements

The rotational motion starts after t*=0.4 and the translational velocity decreases. LEV2 becomes visible in closed streamline forms and the velocity of the vortex core tends to zero. It detaches from the airfoil leading edge, by allowing a new leading edge vortex formation LEV5 at t*= 0.44. The leading edge vortices cover entire upper surface of the airfoil as the angle of attack approaches 90°. The leading edge vortex, LEV5, disappears very quickly due to the rotation of the airfoil towards on it. At t*= 0.48, near to the end of the stroke, the rotational stopping vortex RSV1 is formed. At this time instant the translational vortex TV3 detaches from the trailing edge of the airfoil. After the reversal of the airfoil, at t*= 0.52, the airfoil reenters to the trace of these vortices by pushing RSV1 and TV3 toward downwards and by pushing the traces of LEV3, LEV4 and LEV5 toward upwards.

At t*= 0.56, the new counter-clockwise translational vortex TV1 and the clockwise leading edge vortex LEV1 are formed. The trace of the LEV2 (ccw) is always visible at the mid location of the domain. At the left end of the domain the trace of the TV1 (cw) is also visible. The motion is performed in similar way in the opposite direction. It is noted that, the translational vortex TV1 is clockwise in the left-hand side and counterclockwise in the right hand side of the domain and is highly dominant in the flow-field by inducing a downwash velocity during the whole cycle. After its detachment from the airfoil surface, this translational vortex is visible with closed curved streamlines implying a zero core velocity.

4. Validation of the simulation and physical analysis

4.1 Validation of the numerical simulations

Figure 6 shows the comparison of the velocity and vorticity magnitudes of the PIV measurements and numerical solutions at t*= 0.08, corresponding to the ends of the rotational phase. Same comparison is given in Fig. 7 at t*= 0.28 where the constant velocity translational phase continue. With a general point of view, the same principle structures of vortices and their general topology are distinguishable both in experiment and numerical solutions but it is observed that there exists big abundance of the topology in view of vorticity and *Q* and in experiments.

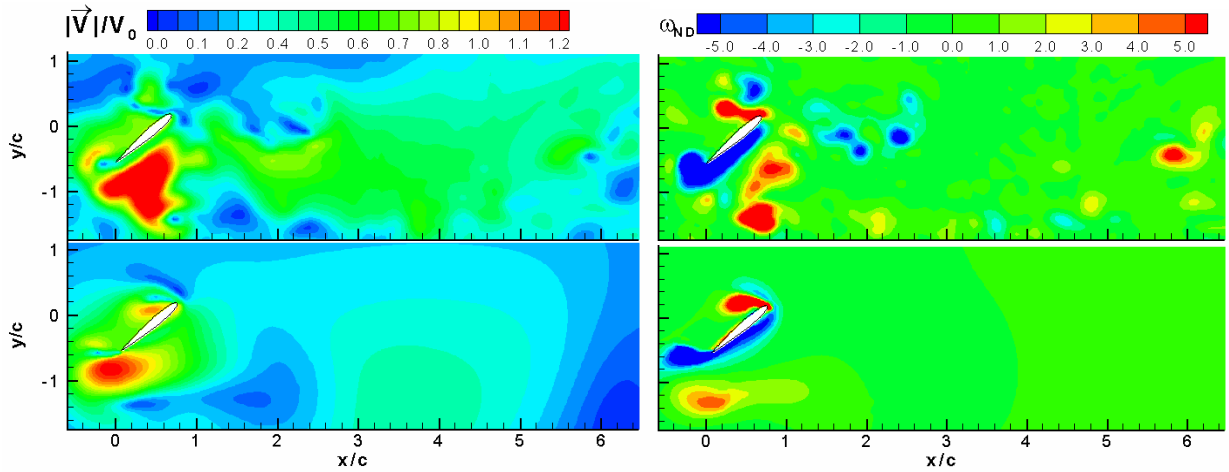

Fig. 6 Instantaneous non-dimensional velocity magnitude (*left column*) and vorticity contours (*right column*) from PIV measurements (*top*) and DNS results (*bottom*) at t*=0.08

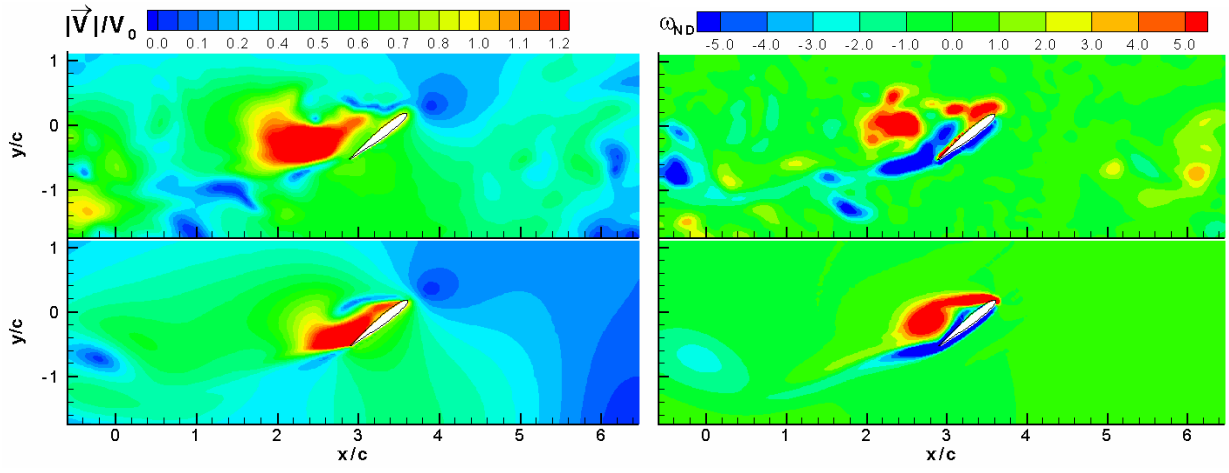

Fig. 7 Instantaneous non-dimensional velocity magnitude (*left column*) and vorticity contours (*right column*) from PIV measurements (*top*) and DNS results (*bottom*) at t*=0.28

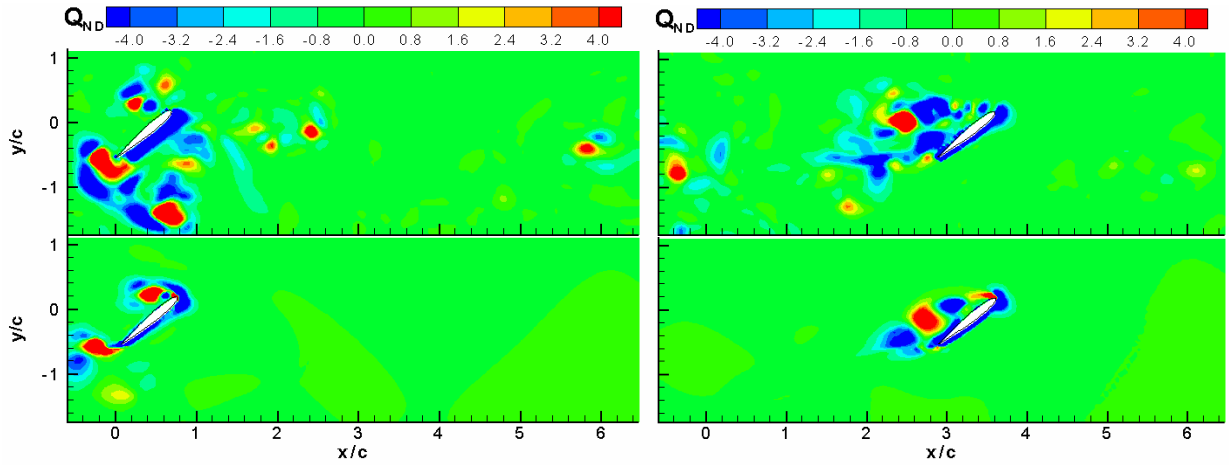

Fig. 8 Instantaneous non-dimensional Q contours at t*=0.08 (*left column*) and at t*=0.28 (*right column*) from PIV measurements (*top*) and DNS results (*bottom*)

With regard to the experimental solutions, we are not sure that the structures stay two-dimensional. This can cause a splitting up of the vortices. The numerical simulations are strictly two-dimensional. The diffusion of vortices in numerical results is too fast and this phenomenon is highly visible during translational phase (Figs. 6-8, bottom rows). The trace of the rotation stays visible in experimental visualizations but disperses in numerical solutions. But also in the numerical solutions, it is observed that the pressure is more persistent (Fig. 9).

The more energetical vortices are highly visible both in numerical solutions, experimental visualizations and PIV measurements, in particular near the airfoil. They are also influencing the aerodynamic forces on the airfoil. The aerodynamic forces are mostly dependent on the vortices close to the airfoil which also influences the pressure values on the airfoil surface. The two-dimensional analysis of numerical solutions reveals obviously the presence of these most energetical vortices which are close to the wake but the vortices disappear too fast to interact with the following stroke in the far field.

4.2 Physical analysis

At the end of the rotation (t*=0.08), on the upper surface of the airfoil there is two suction regions resulted from the LEV1 and TV1 (Fig. 9). Since Q is the Laplacian of the pressure (Jeong and Hussain 1995; Dubief and Delcayre 2000), it is noted that the centers of the vortices are the centers of suction peaks (Fig. 8, left column). Lower surface of the airfoil is surrounded with a shear region where the Q values are negative. Stagnation point is at the lower surface of the airfoil and is very close to the leading edge. Lift coefficient is approximately equal to the drag coefficient at this time so the resultant force is approximately normal to the airfoil. From, t*=0.13 to t*=0.16, during translational phase, there is a slight increase of the lift coefficient (C_L) and drag coefficient (C_D) as shown in Fig. 10. From the visualization, it is observed that the trailing edge vortex, TV1, moves away from the airfoil and the leading edge vortex is dominant on the upper surface of the airfoil (Fig. 9). The lift coefficient is also approximately equal to the drag coefficient. From t*=0.16 to t*=0.36, the lift and drag coefficients decrease, where the suction pressure region displaced from the leading upper surface of the airfoil towards its trailing upper surface. In the same time, the influence of the overpressure region at the lower surface of the airfoil diminishes.

The Eulerian acceleration magnitudes obtained from PIV measurements during translational phase are represented in Fig. 11. At t*=0.36, a separation phenomena during the translational phase is observed. A weak counter rotating vortex is generated on the upper surface of the airfoil. Negative pressure region on the upper surface of the airfoil also moves from the leading edge toward to the trailing edge. Lift coefficient reaches its first minimum at this time.

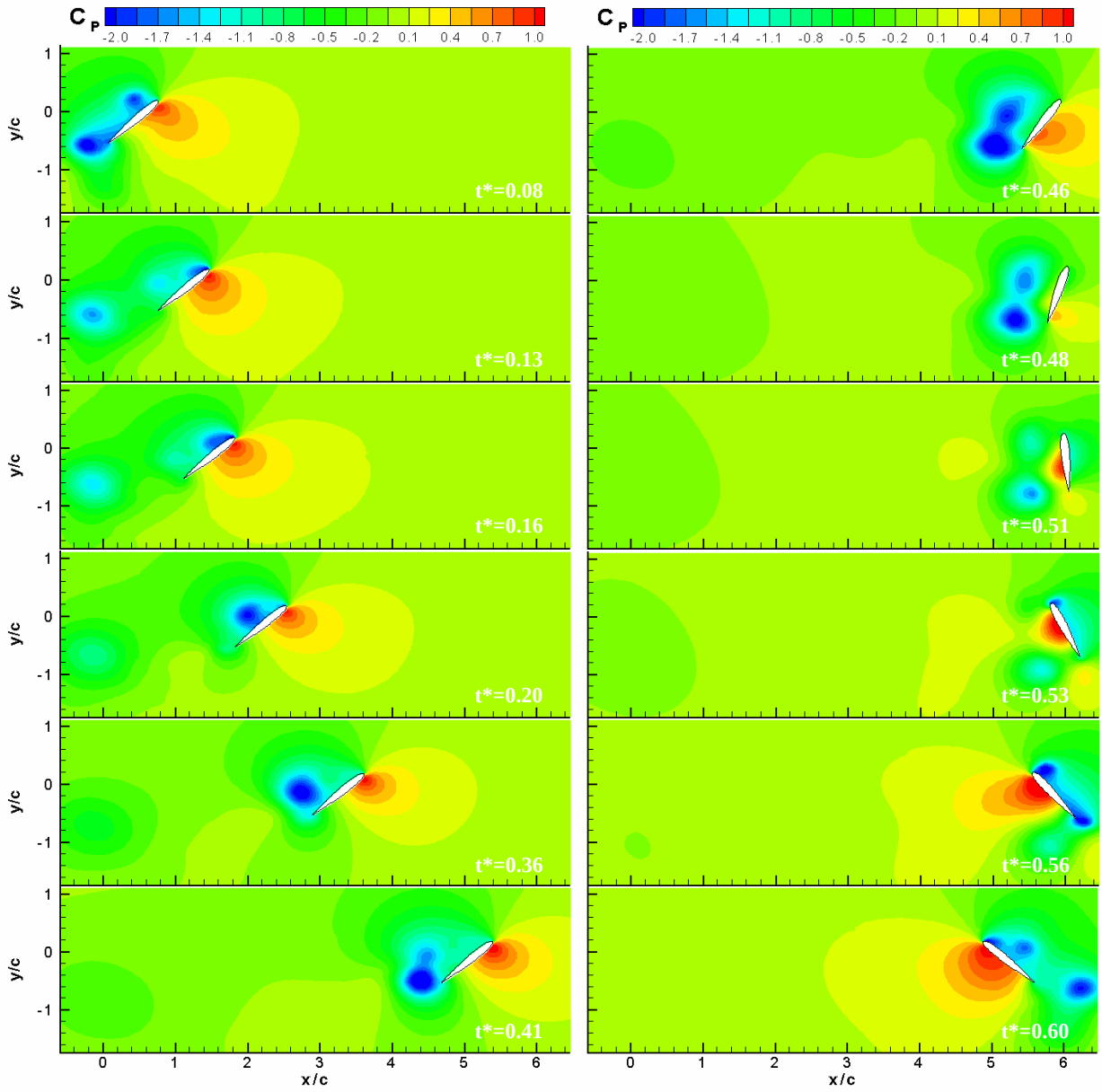

Fig. 9 Instantaneous pressure coefficient (C_P) contours from DNS results

At the beginning of the rotation (t*= 0.41), the rotation reinforces the vortex at the trailing edge and weakens the vortex at leading edge. The suction region is situated at the trailing edge of the airfoil. As the angular velocity increases and angle of attack approaches to 90°, these suction peaks grow and spread out toward the leading edge. The suction region on the upper surface of the airfoil becomes stronger. After a while, the pressure regions are detached from the airfoil upper surface. Firstly, the leading edge vortex region moves away from the airfoil as seen from the pressure contours at t*= 0.46 (Fig. 9) and then the trailing edge suction region moves away from the airfoil surface at t*=0.48. At the end of a stroke (t*= 0.5), when the airfoil is 90° angle of attack the influence of the two big vortices on the airfoil vanishes. The airfoil is moving away of these two vortices resulting with zero lift and drag coefficient values in numerical simulations, which is seen also on the pressure contours close to the airfoil (Fig. 9). This phenomenon is also visible in PIV measurements. The lift and drag coefficients are equal to zero at the end of the stroke. At the beginning of the second stroke (t*= 0.51), the traces of the two big vortices are always present and could be seen by the two levels of suction regions. The airfoil is accelerating in this region. The pressure on the lower surface of the airfoil starts to increase. This overpressure helps to eject the two suction zones one towards downwards and the other one toward upwards. As a result, there is a

very small interaction between these two suction regions and the airfoil.

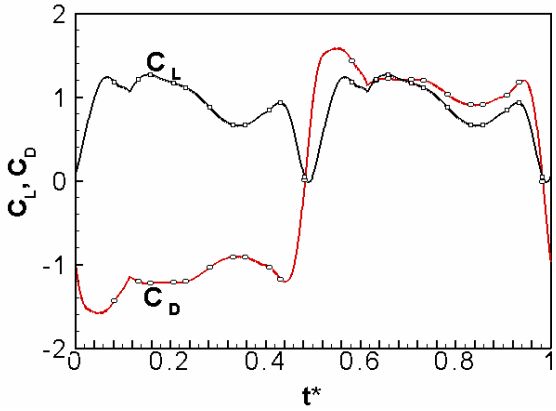

Fig. 10 Instantaneous aerodynamic force coefficients from DNS results

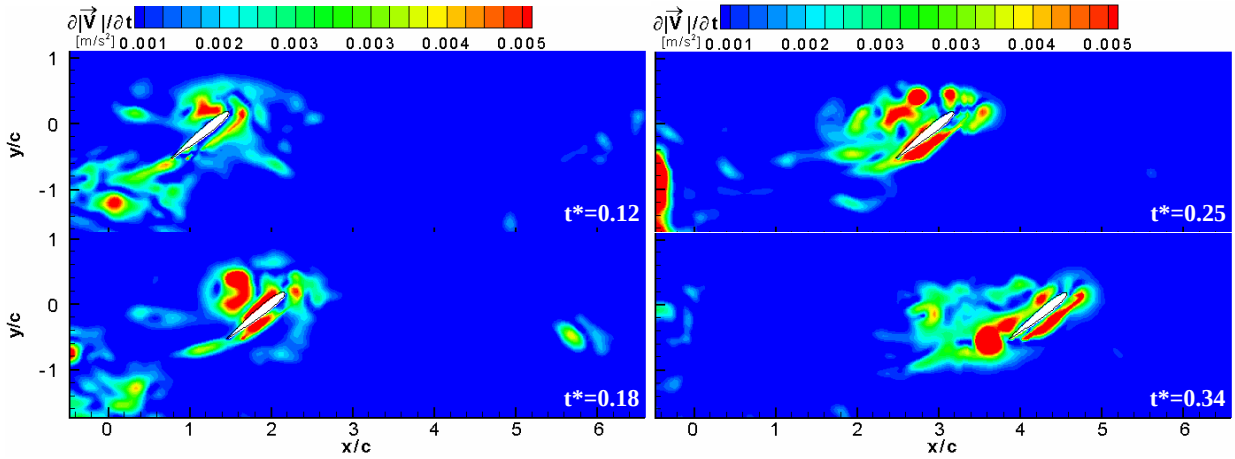

Fig. 11 Instantaneous Eulerian acceleration magnitudes from PIV measurements.

As going from t*= 0.36 to t*= 0.51, the lift and drag coefficients decreases until zero value at the end of the stroke. The two suction center of the vortex created during the previous stroke is ejected by the newly created overpressure region. This results a positive lift during the whole flapping motion (t*= 0.53). From t*= 0.53 to t*= 0.56, the lift and drag coefficients increase, and the lift coefficient reaches its maximum at t*= 0.56. At t*= 0.6, the rotational phase finishes and the constant velocity translational phase restarts.

5. Conclusions and perspectives

A complex instantaneous vortex dynamics is investigated due to a proposed flapping motion. The instantaneous flow topology shows the interaction of the vortices generated with the trace of the vortices from the previous stroke. The PIV measurements and the laser sheet visualizations are used in order to identify these vortices generated during different phases of the flapping motion. There is a good agreement between different types of visualizations in phenomenological point of view. Three different types of vortices are observed namely Leading Edge Vortex (LEV) generated at the leading edge of the airfoil, Translational Vortex (TV) generated at the trailing edge of the airfoil during the translational phase of the motion and the Rotational Stopping Vortex (RSV) at the trailing edge of the airfoil generated during the rotational phase. The more energetical vortices are highly visible both in experimental visualizations and numerical simulations and these are the vortices which influence more the aerodynamic forces on the airfoil. The trace of the rotation stays visible in experimental visualizations while there is a quick diffusion in numerical simulations. Experimental results give more complicated topology compared to numerical simulations. From the

conclusion of this comparison, it seems to be necessary to perform an experimental parametrical study in order to investigate the influence of different parameters, such as angle of attack α_0, position of the velocity change x_v, position of the angle of attack change x_a. The calculation of the instantaneous aerodynamic forces by using PIV measurements (Kurtulus et al. 2006) will yield complementary information on aerodynamic force predictions of flapping motion studies.

Acknowledgements

This work was supported by ENSMA, METU, TUBITAK, CNRS and French Ambassy in Turkey. Their supports are greatly acknowledged. Miss. Funda Kurtulus thanks also to Zonta International Foundation (USA) to select her as an Amelia Earhart Fellow of 2005.

References

Azuma A, Azuma S, Watanabe I, Furuta T (1985) Flight mechanics of a dragonfly. J Exp Biol 116: 79–107

Dickinson MH (1994) The effects of wing rotation on unsteady aerodynamics performance at low Reynolds numbers J Exp Biol 192:179-206

Dubief Y, Delcayre F (2000) On coherent-vortex identification in turbulence. J Turbulence 1:1-22

Dudley R. (1998) The biomechanics of insect flight: form, function, evolution. Princeton: Princeton Univ. Press

Ellington CP (1984) The aerodynamics of hovering insect flight I. The quasi-steady analysis. Philos Trans R Soc London Ser B 305:1–15

Hamdani H, Sun M (2000) Aerodynamic forces and flow structures of an airfoil in some unsteady motions at small Reynolds number. Acta Mechanica 145:173-187

Jeong J, Hussain F (1995) On the identification of a vortex. J. Fluid Mech 285:69-94

Koochesfahani MM (1989) Vortical patterns in the wake of an oscillating airfoil AIAA J 27:1200-1205.

Kurtulus DF, Farcy A, Alemdaroglu N (2005) Unsteady aerodynamics of flapping airfoil in hovering flight at low Reynolds numbers. AIAA 2005-1356 Reno Nevada

Lai J, Platzer MF (2001) Characteristics of a plunging airfoil at zero freestream velocity. AIAA J 39:531-534

Nachtigall W (1974) Insects in Flight. New York: McGraw-Hill

Norberg UM (1985) Evolution of vertebrate flight: an aerodynamic model for the transition from gliding to active flight. Am Nat 126:303–27

Pennycuick CJ. (1988) On the reconstruction of Pterosaurs and their manner of flight, with notes on vortex wakes. Biol Rev 63:299–331

Ramamurti R, Sandberg WC (2002) A three-dimensional computational study of the aerodynamic mechanisms of insect flight. J Exp Biol. 205:1507-1518

Rayner JMV (1979) A vortex theory of animal flight. Part 1. The vortex wake of a hovering animal. J Fluid Mech 4:697–730

Rayner JMV (1985) Vertebrate flapping flight mechanics and aerodynamics, and the evolution of flight in bats. Biona Rep 5:27–74

Platzer MF, Jones KD (2006) Flapping Wing Aerodynamics - Progress and Challenges. AIAA-2006-0500, Jan. 2006, Reno, Nevada

Kurtulus DF, Scarano F, David L (2006) Unsteady aerodynamic forces estimation on a square cylinder by TR-PIV (submitted to Exp in Fluids)

Shyy W, Berg M, Ljungqvist D (1999) Flapping and Flexible Wings for Biological and Micro Air Vehicles. Prog Aerospace Sci 35:455-505